



ZnO-gCN Coated Separator for Modulating the Solid-Electrolyte Interphase on Lithium Metal Anodes

Rashmi Yadav, Ankush Kumar Singh, and Rosy*

Lithium metal batteries are recognized as potential candidates for the next-generation energy storage system. Nevertheless, their chemical reactivity, volumetric changes, and dendritic deposition profoundly influence their performance. Introducing an artificial solid-electrolyte interphase (ASEI) is one of the most effective ways to tackle this interfacial instability. However, due to unparalleled reactivity, the direct interfacial engineering of lithium is challenging. Herein, the modification of the polypropylene (PP) separator with lithophilic zinc oxide (ZnO) and graphitic carbon nitride (gCN) is reported as an indirect yet effective strategy to tackle the interfacial instability of lithium. This work substantiates that ZnO.gCN PP modulates the electrolyte uptake, ionic conductivity, and Li⁺

transportation and reacts with the lithium metal to form an ASEI having rigid inorganic materials, leading to much lower nucleation overpotential, reduced polarization, and remarkable cycling stability of more than 500 cycles at 1 mA cm⁻². The GITT studies further manifested the improved mass and charge-transfer kinetics of Li⁺ in the presence of ZnO.gCN PP. The postcycling high-resolution scanning electron microscopy and X-ray photoelectron spectroscopy analysis confirmed that the enhanced electrochemical performance resulted from uniform Li plating/stripping and suppressed electrolyte degradation. Furthermore, the practicality of ZnO.gCN PP is demonstrated through the significantly improved electrochemical performance of NCM811.

1. Introduction

Since the 1990s, lithium-ion batteries have attracted considerable attention and have established themselves as the leading choice for commercial power sources due to their outstanding performance and reliability, such as high-energy density, long lifespan, high coulombic efficiencies, and stable voltage profile.^[1,2] With the advancement of electric vehicles and smart grid storage, the need for high-energy-density storage systems has become more urgent. The incredibly high theoretical specific capacity (3860 mAh g⁻¹) and low electrochemical potential (-3.04 V vs. SHE) of lithium metal anode make it suitable for next-generation state of the art lithium metal batteries.^[1,3,4] Despite the high-energy density feature, Li metal has the highest safety risk among all types of anode materials, which stems from the uncontrolled growth of Li dendrites.^[5-8] During the plating and stripping process, lithium undergoes significant electrochemical and chemical reactions with the nonaqueous electrolyte, forming a solid-electrolyte interphase (SEI). Over time, this SEI layer accumulates, cracks, and exposes fresh lithium, which then reacts further with the electrolyte and offers preferential sites for the deposition of incoming Li⁺, leading to mossy and dendritic non-uniform lithium plating.^[9-11] The formation of Li dendrites results in dendrite-induced internal short circuits, aggravated chemical reaction between Li metal and electrolyte, accumulated dead Li, increased

cell polarization, and significant volume changes during continuous plating/stripping. These factors contribute to the reduced capacity, low coulombic efficiency, and short lifespan, which hinders the commercial deployment of lithium metal anode. Hence, developing a stable electrode/electrolyte interphase is essential to suppress dendrite formation and utilize lithium metal as high-energy anodes.^[2,12]

In recent years, various approaches have been developed to enhance the stability of lithium anodes. Forming an ASEI is one of the most promising and practical approaches.^[13-15] Typically, inorganic metal oxides (Al₂O₃, ZnO, MgO), flexible polymers (LiPON, PVDF, PDMS), and rigid ceramics (ZnF₂, LiF, Li₃PO₄) have been previously adopted to create a nanoscale passivation layer on lithium metal.^[6,16-18] Though these ASEIs were beneficial in stabilizing the metal anode, they have been designed to act only as a mechanical barrier between the highly reductive electrolyte and metal anode without contributing much to the chemical and electrochemical properties. Furthermore, due to metallic lithium's unparalleled reactivity, sophisticated techniques like atomic/molecular layer deposition (MLD),^[19,20] magnetron sputtering,^[21] dip coating,^[22] cast coating^[23] and chemical vapor deposition have been employed to produce nanoscale, homogeneous ASEIs on lithium anodes.^[13,14,24,25] Chen et al. utilized atomic layer deposition to create LiF thin film using tBuOLi and HF.^[26] Sun et al. applied MLD to form a polyurea coating with ethylenediamine and 1,4-phenylene diisocyanate.^[27] Coatings of MoS₂,^[28] Al₂O₃,^[29] and Li₃PO₄^[30] were successfully deposited onto lithium foil through either electron beam or magnetron sputtering techniques. The solid-gas reaction method was reported to generate an in situ ASEI layer consisting of Li₂S^[31] and Li₃N^[32] from sulphur vapor and nitrogen, respectively. Wu et al. demonstrated a solid-solution reaction to create a uniform composite film of LiF and polymer on lithium by reacting PVDF in DMF.^[33] Nazar and

R. Yadav, A. K. Singh, Rosy

Department of Chemistry

Indian Institute of Technology (Banaras Hindu University) Varanasi
Uttar Pradesh 221005, India

E-mail: ros.y.chy@iitbhu.ac.in



Supporting information for this article is available on the WWW under <https://doi.org/10.1002/batt.202500128>

colleagues described a simple surface chemistry process for the direct reduction of metal chlorides and metal salts with lithium at room temperature.^[34] Additionally, incorporating additives such as HF, Al₃,^[35] and carbonate^[36,37] into the electrolyte may offer a potential strategy for developing a protective film, yet achieving effective passivation between the lithium metal anode and the electrolyte remains a significant challenge. The cost point of view impedes the large-scale adoption of these techniques. Interestingly, the electrode/electrolyte interphase at the highly reactive lithium anode can be modulated simply by using the separators modified with a rational selection of materials. Separators being in direct contact with the anode and the electrolyte, when modified with the lithophilic materials, can influence the Li⁺ transportation and react with the lithium surface to facilitate ASEI formation. Additionally, the separator modification can potentially address the low thermal stability and poor electrolyte wettability of commercial polyolefin separators.^[18,38]

Along the same line, here in this work, the interfacial instability of lithium metal anodes has been tackled by modifying the separator with lithophilic zinc oxide (ZnO) and graphitic carbon nitride (gCN). This modification aims to promote uniform Li⁺ plating and stripping, effectively suppressing dendrite formation and extending the battery's lifespan. The lithophilic nature of ZnO will promote the *in situ* formation of mechanically robust SEI composed of Zn and ZnF₂.^[39,40] In contrast, the polymeric N-rich nature of gCN will offer abundant N-sites promoting strong interactions with Li⁺ and the formation of Li-N bonds, ultimately resulting in uniform Li⁺ flux through the separator and altered SEI. Additionally, the intrinsic structural characteristic of gCN will provide nanochannels that can modulate Li⁺ ion transport, further improving electrochemical performance at higher current densities.^[41–43] The ZnO.gCN coated polypropylene separator (ZnO.gCN PP) thus offers a straightforward strategy to form ASEI composed of ZnF₂, ZnO, Li-N, and residual ZnO.gCN, *in situ*. Owing to the high shear/Young's modulus and lithophilic nature of these components, the ZnO.gCN PP will facilitate the Li⁺ nucleation, minimize the interfacial instability, and homogenize the Li⁺ flux, resulting in reduced overpotential, enhanced cycle life, and improved coulombic efficiency of the lithium metal anode.

2. Results and Discussions

2.1. Characterization of ZnO.gCN Engineered Separator

The ZnO.gCN-modified separator was prepared by allowing self-assembly/adsorption of the ZnO.gCN composite onto the polypropylene separator (PP 2500), as discussed in the experimental section. The modification turned the translucent separator to light brownish due to the adsorption of a brownish ZnO.gCN composite. HR-SEM images of the bare and modified separators were captured to visualize the changes in the surface morphology. Figure 1a presents the porous structure of the bare separator as reported by Celgard. In contrast, all the modified PP separators (Figure 1b and Figure S2a,b, Supporting Information) were found to be decorated with nanoscale ZnO.gCN structures. The porous surfaces of both 1:1 and 3:1 ZnO.gCN were fully decorated with the flake-like structures

of ZnO.gCN. In addition to the pores, abundant nanochannels were observed from the inherent framework of ZnO.gCN. The elemental mapping for 3:1 ZnO.gCN PP shows the distribution of C, N, O, and Zn all over the surface, affirming the surface decoration with ZnO.gCN (Figure S3, Supporting Information).

Thermal stability is a crucial characteristic of a separator. A separator with a low melting point is prone to melting and shrinking during battery operation, which can lead to pore obstruction and disrupt ion transport between the electrodes, ultimately affecting the electrochemical performance. Hence, it is essential to enhance or at least maintain the thermal stability of the separator during the modification process. Therefore, the effect of surface modification on the thermal stability and thermal shrinkage of the PP separator was investigated by employing heat treatment and TGA. The thermal shrinkage of both the bare and modified separators was evaluated by exposing the separators to 50 °C and 100 °C for 1 h. Comparative images of the PP separators exposed to various temperatures are presented in Figure 1c. All the separators exhibited intact dimensions when subjected to 50 °C. However, as the temperature increased to 100 °C, the bare PP rolled up, showcasing crumpled edges. The 1:1 and 1:3 ZnO.gCN PP were also found to be rolled to different extents. In contrast, the 3:1 ZnO.gCN PP showed unnoticeable shrinkage at 100 °C, demonstrating superior resistance to thermal shrinkage. Figure 1d presents the TGA curves for bare and 1:1 ZnO.gCN PP, 1:3 ZnO.gCN PP, and 3:1 ZnO.gCN PP. The TGA results show that the bare separator begins to experience weight loss at 329 °C, while the onset temperatures for the 1:1 ZnO.gCN, 1:3 ZnO.gCN, and 3:1 ZnO.gCN separators occur at 326, 355, and 345 °C, respectively. The elevated onset temperatures of the modified separators suggest enhanced thermal stability, which can be ascribed to the superior thermal stability of both ZnO and gCN. Figure S4, Supporting Information represents the corresponding derivative (DTG) curve, which describes the decomposition stages of the bare and modified PP.

After ensuring the thermal stability, the impact of surface modification on electrolyte uptake was assessed using Equation (1). As presented in Table 1, the 3:1 ZnO.gCN separator exhibits an electrolyte uptake of 542.3%, whereas the bare PP separator shows a lower uptake of 414.2%. The higher electrolyte uptake of the 3:1 ZnO.gCN-modified separator suggests an improved ability to absorb and retain the electrolyte, which is anticipated to significantly enhance its ionic conductivity. This increased uptake can facilitate better mass transportation within the separator, ultimately improving overall performance. Therefore, after assessing the electrolyte uptake, the ionic conductivity was measured using Equation (2). EIS was performed over a frequency range of 0.1 MHz–1 Hz, with two separators, each soaked in electrolyte for 1 h and sandwiched between stainless steel current collectors. The Nyquist plot for the bare and ZnO.gCN-modified separators is shown in Figure 1e. The bulk resistance (R_b) obtained from the Nyquist plot was used to calculate the ionic conductivity, which was found to be 1.1 mS cm⁻¹ for the bare PP separator and 1.47, 1.54, and 2.03 mS cm⁻¹ for the 1:1 ZnO.gCN PP, 1:3 ZnO.gCN PP, and 3:1 ZnO.gCN PP separators, respectively (Table 1).

The results from the aforementioned studies demonstrate that the 3:1 ZnO.gCN separator exhibits superior thermal stability, reduced thermal shrinkage, higher electrolyte uptake, and

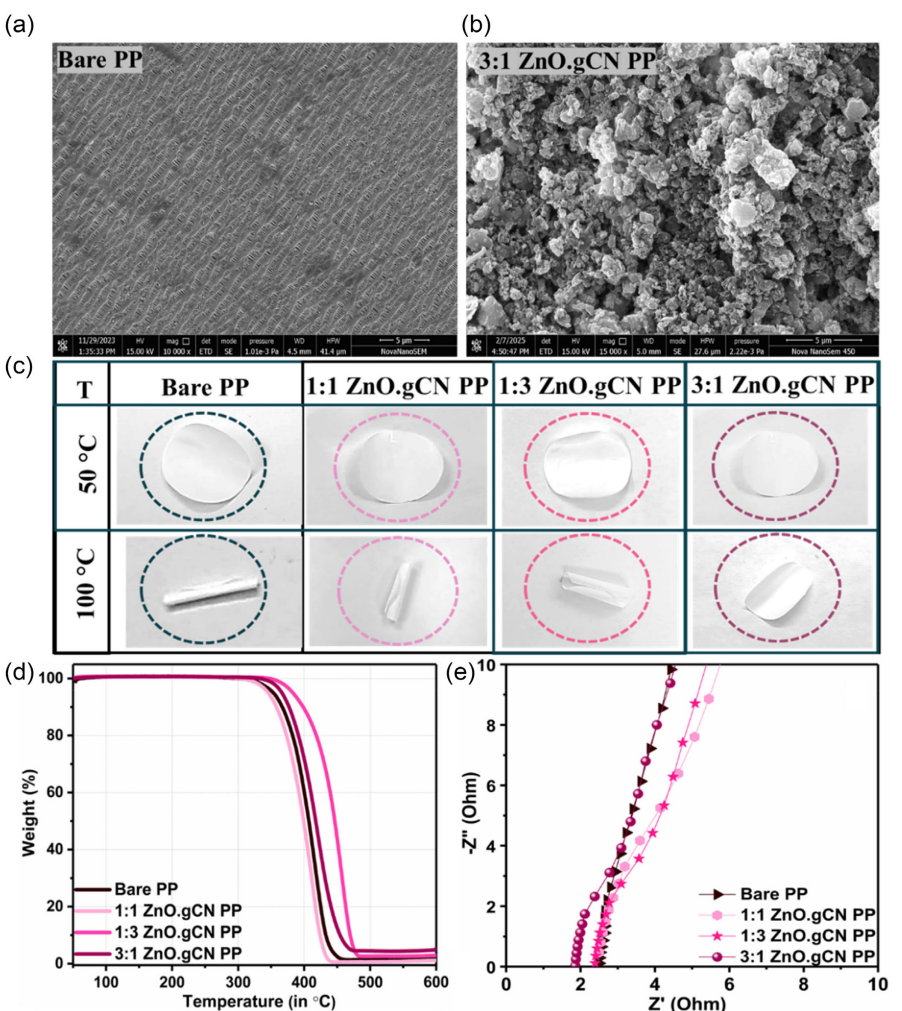


Figure 1. HR-SEM images of a) Bare PP and b) 3:1 ZnO.gCN PP. Comparative c) Thermal shrinkage, d) TGA plots, and e) Nyquist plot for bare and modified separator.

Table 1. Electrolyte uptake percentage and ionic conductivity values of the bare and ZnO.gCN modified separator.

Separators	Electrolyte Uptake [%]	Ionic Conductivity [σ]	Thickness [d]	Weight
Bare PP	414.2	1.10 mS cm $^{-1}$	36.0 μ m	2.80 mg
1:1 ZnO.gCN PP	456.1	1.47 mS cm $^{-1}$	37.0 μ m	3.03 mg
1:3 ZnO.gCN PP	498.4	1.53 mS cm $^{-1}$	37.0 μ m	3.06 mg
3:1 ZnO.gCN PP	542.3	2.03 mS cm $^{-1}$	38.0 μ m	3.10 mg

enhanced ionic conductivity compared to the bare PP and other modified separators. These improvements suggest that the incorporation of a lithiophilic and nitrogen-rich ZnO.gCN layer effectively enhances the thermal endurance and Li $^{+}$ diffusion through the modified separator. Subsequently, these separators were deployed in symmetrical cells to study their impact on the lithium plating and stripping behavior.

2.2. Electrochemical Testing

The effect of ZnO.gCN PP modification on lithium metal stripping and plating behavior was systematically investigated by

constructing Li|Li symmetrical cells incorporating both modified and unmodified PP separators. The symmetrical cell having bare PP separators showcases a nucleation overpotential of 227 mV at 0.2 mA cm^{-2} , which was found to be 145 mV higher than the growth overpotential. In contrast, with the 3:1 ZnO.gCN PP, a significantly lower nucleation overpotential of 113 mV was observed, which was only 45 mV higher than the growth overpotential (Figure 2a). This substantially reduced difference between the nucleation and growth overpotential suggests that ZnO.gCN can modulate Li deposition by facilitating nucleation through its lithiophilic properties and enhanced wettability, resulting in uniform Li $^{+}$ flux. Li|Li cells were tested under varying areal current

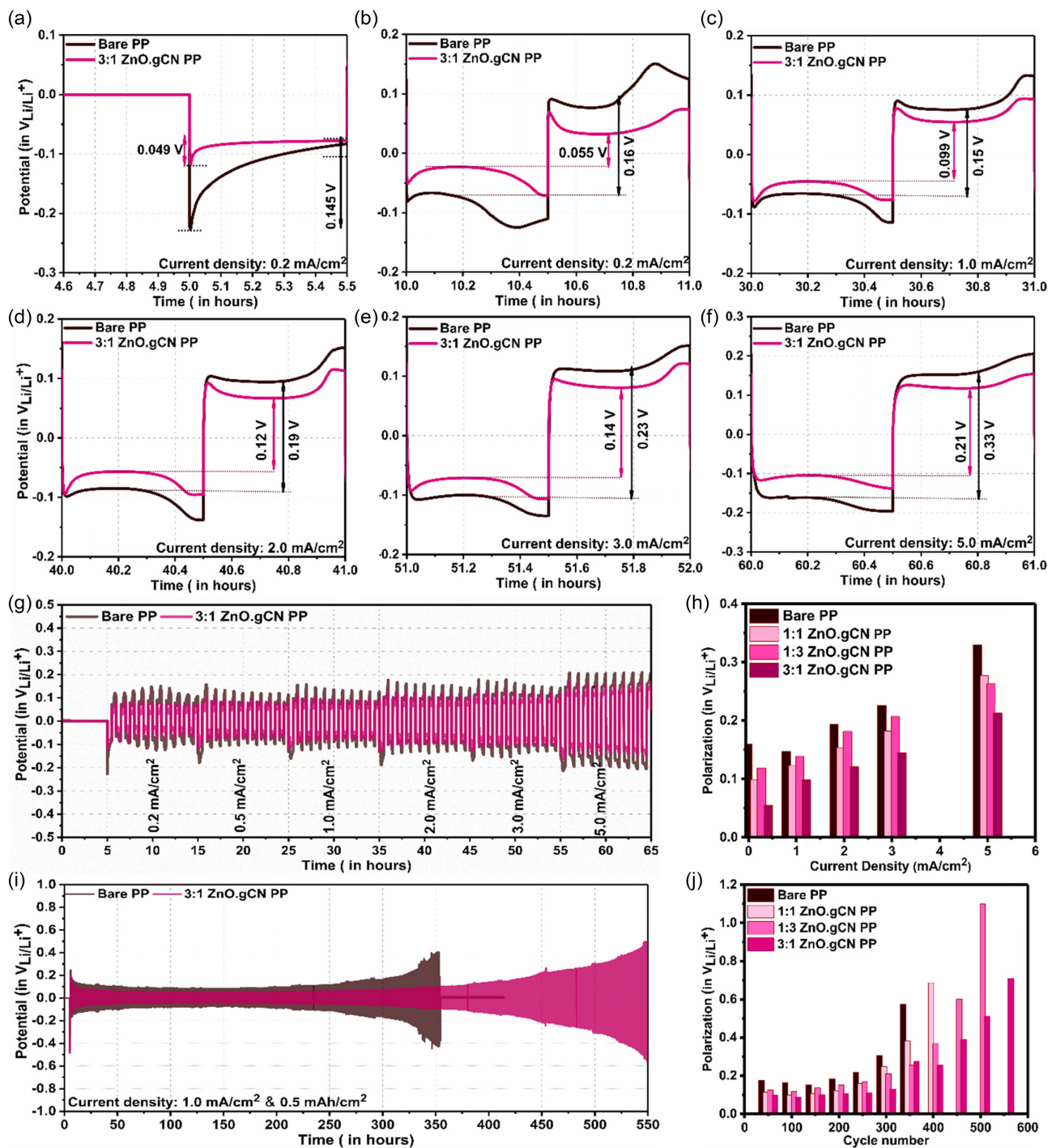


Figure 2. Comparative voltage profiles observed during electrochemical testing of Li||Li symmetrical cells at a,b) 0.2 mA cm⁻², c) 1 mA cm⁻², d) 2 mA cm⁻², e) 3 mA cm⁻², f) 5 mA cm⁻². Comparative g) Voltage profile and h) corresponding increase in voltage polarization at different current densities. Comparative i) cycling performance and j) corresponding increase in polarization as a function of cycle number.

densities ranging from 0.2 to 5 mA cm⁻² to comprehensively understand the role of modified PP separators. The time-dependent galvanostatic charge-discharge profiles at varying areal current densities are shown in Figure 2b-h and Figure S5, Supporting Information. All ZnO.gCN-modified separators exhibited lower voltage polarization compared to bare PP separators. As the current density increased from 0.2 to 5 mA cm⁻², the plating-stripping polarization for the cell with an unmodified

separator rose from 160 to 330 mV. In contrast, all the modified separators showcased lower voltage hysteresis with 1:1 ZnO.gCN PP rose from 99 mV to 277 mV, 1:3 ZnO.gCN PP increased from 120 to 263 mV and 3:1 ZnO.gCN PP ascended from 55 to 210 mV. The lowest voltage hysteresis of 3:1 ZnO.gCN compared to all other modified and unmodified PP manifested its superior plating/stripping stability and reversibility over all the tested current densities.

Following the rate performance test, the cycling stability of the symmetrical cells was assessed at a current density of 1 mA cm^{-2} and a capacity of 0.5 mAh cm^{-2} . As shown in Figure 2i and Figure S5(i), Supporting Information, the voltage hysteresis of the symmetrical cells with bare PP and 1:1 ZnO.gCN separators increased rapidly, with the bare PP cell short-circuiting at the 335th cycle, followed by the 1:1 ZnO.gCN cell at approximately the 390th cycle. The cell with the 1:3 ZnO.gCN separator remained stable up to 425 cycles, with minimal polarization increase, after which the voltage hysteresis began to rise sharply, leading to cell shorting at 503rd cycle. In contrast, the 3:1 ZnO.gCN cell exhibited the lowest initial voltage hysteresis of 98 mV. The polarization slightly increased after the 400th cycle. The evolution of cell polarization with cycle number is presented in Figure 2j. The figure clearly shows that the use of 3:1 ZnO.gCN allows stable plating striping behavior for more than 500 cycles in a corrosive carbonate-based electrolyte solution with a minimum evolution of voltage hysteresis, showcasing nearly 69% higher cycle life compared to the cell having bare PP. This performance enhancement results from superior electrolyte wettability, higher ionic conductivity, and improved interfacial stability exerted by the 3:1 ZnO.gCN separator.

For comparison, the reversibility of lithium plating-stripping behavior in the presence of ZnO PP was also investigated at a current density of 1.0 mA cm^{-2} , and the results are presented in Figure S6, Supporting Information. The cell containing ZnO PP maintained stable polarization up to the 375th cycle, after which the polarization began to rise, resulting in a short circuit around the 440th cycle. The ZnO PP demonstrated appreciable improvement. Nonetheless, the polarization and cycling stability of the 3:1 ZnO.gCN PP were much better than the ZnO PP, highlighting the superiority of the 3:1 ZnO.gCN PP over ZnO PP.

Next, a range of experiments, including linear polarization (Tafel) measurements, chronoamperometry, and the Galvanostatic Intermittent Titration Technique (GITT), were conducted to thoroughly evaluate the impact of 3:1 ZnO.gCN PP on the kinetic performance of the lithium plating/stripping in Li|Li symmetrical cells. The exchange current density (i_0), an essential parameter for evaluating the lithium-ion diffusion kinetics at the electrode/electrolyte interphase, was measured by analyzing the Tafel plot recorded using Li|Li symmetric cells having bare and 3:1 ZnO.gCN PP, respectively. As presented in Figure 3a, the cell with 3:1 ZnO.gCN PP exhibits an exchange current density of 0.53 mA cm^{-2} , which is 1.4 times higher compared to 0.38 mA cm^{-2} exhibited by the cell having bare PP, indicating faster Li^+ transfer kinetics in the presence of ZnO.gCN.^[44] The substantially higher exchange current density can be attributed to the uniform distribution of Li^+ ions through the open nanopore channels of ZnO.gCN, which ensures an adequate supply of Li^+ ions for deposition, thereby facilitating the kinetics in the proximity of the anode. Next, the lithium-ion transference number (t_{Li}^+) for both 3:1 ZnO.gCN PP and bare PP electrodes was evaluated. The t_{Li}^+ is a critical parameter for understanding the efficiency of lithium-ion movement through electrolyte membranes. A higher transference number indicates a reduced likelihood of side reactions, as well as an extended battery lifespan. The transference number for 3:1 ZnO.gCN PP, as calculated from the data shown in Figure 3b and Figure S7, Supporting Information, was

found to be 0.67, which is significantly higher than the 0.44 observed for bare PP. This suggests faster lithium-ion migration and a more uniform lithium-ion distribution across the 3:1 ZnO.gCN PP interphase.^[45–47] During continuous charging and discharging, the dead Li layer keeps on accumulating, resulting in increased thickness of the diffusion layer across the electrode/electrolyte interface. This accumulation of dead Li thus leads to mass transport limitations during cell cycling, impeding lithium-ion transport.^[46,48] Therefore, the accumulation of the dead lithium and its effect on mass transport and the reaction kinetics of Li|Li symmetric cells was next investigated using the GITT, as shown in Figure 3c.

The GITT measurements were conducted at 1 mA cm^{-2} following a sequence of 15 galvanostatic cycles. Each GITT cycle comprised of 20 discharge cycles, followed by 20 charge cycles, with a brief current pulse duration of 15 sec and a rest period of 3 min. This approach allowed for a detailed analysis of the electrochemical kinetics by providing insights into the diffusion and transport processes of lithium ions during cycling. Figure S8, Supporting Information illustrates the initial GITT cycle for both bare and modified PP, showing nearly identical polarization profiles when compared to their earlier galvanostatic cycle. This suggests that mass transport has a minimal impact on polarization during the initial cycles. As the GITT cycles advance from the second cycle (Figure 3d) and then to the fifth cycle (Figure 3e), the polarization observed in both cells is reduced. Nonetheless, the percentage reduction in overpotential between the previous galvanostatic cycle and the GITT 2nd cycle was 14.6% for bare PP and 4.6% for 3:1 ZnO.gCN PP. By the 5th GITT cycle, the reduction in overpotential increased to 26% for bare PP and 18% for 3:1 ZnO.gCN PP. Nevertheless, the 3:1 ZnO.gCN PP continually shows a considerably lower overpotential compared to bare PP, suggesting more pronounced mass transfer limitations in the case of bare PP, which majorly arise from the accumulation of dead lithium. These GITT results align with previous findings, which demonstrate enhanced ionic conductivity and a higher exchange current density for Li^+ in the presence of the 3:1 ZnO.gCN PP and explain its superior electrochemical performance.

2.3. Postcycling Analysis

To explore the underlying factors contributing to the enhanced electrochemical performance, extended cycle life, and reduced voltage hysteresis in lithium plating/stripping with ZnO.gCN, the surface composition of cycled lithium anodes was investigated. XPS and HR-SEM techniques were employed to examine the composition of the SEI and the morphology of the lithium anode.

The XPS analysis of lithium cycled in the presence of 3:1 ZnO.gCN (ZnO.gCN|Li) showcased the presence of zinc and nitrogen, indicating the modulation of SEI with ZnO and gCN-related chemical moieties. The deconvoluted Zn 3d spectra presented in Figure 4a reveal three peaks at 9.3, 11.2, and 12.7 eV, corresponding to Zn, ZnO, and ZnF₂, respectively.^[49] Additionally, the deconvoluted N 1s spectra shown in Figure 4b exhibited four peaks. The peaks at 399.23, 400.6, and 403.7 eV correspond to the bridging N atoms in N-(C)₃ (triazine ring constituting gCN), N—H bonds,

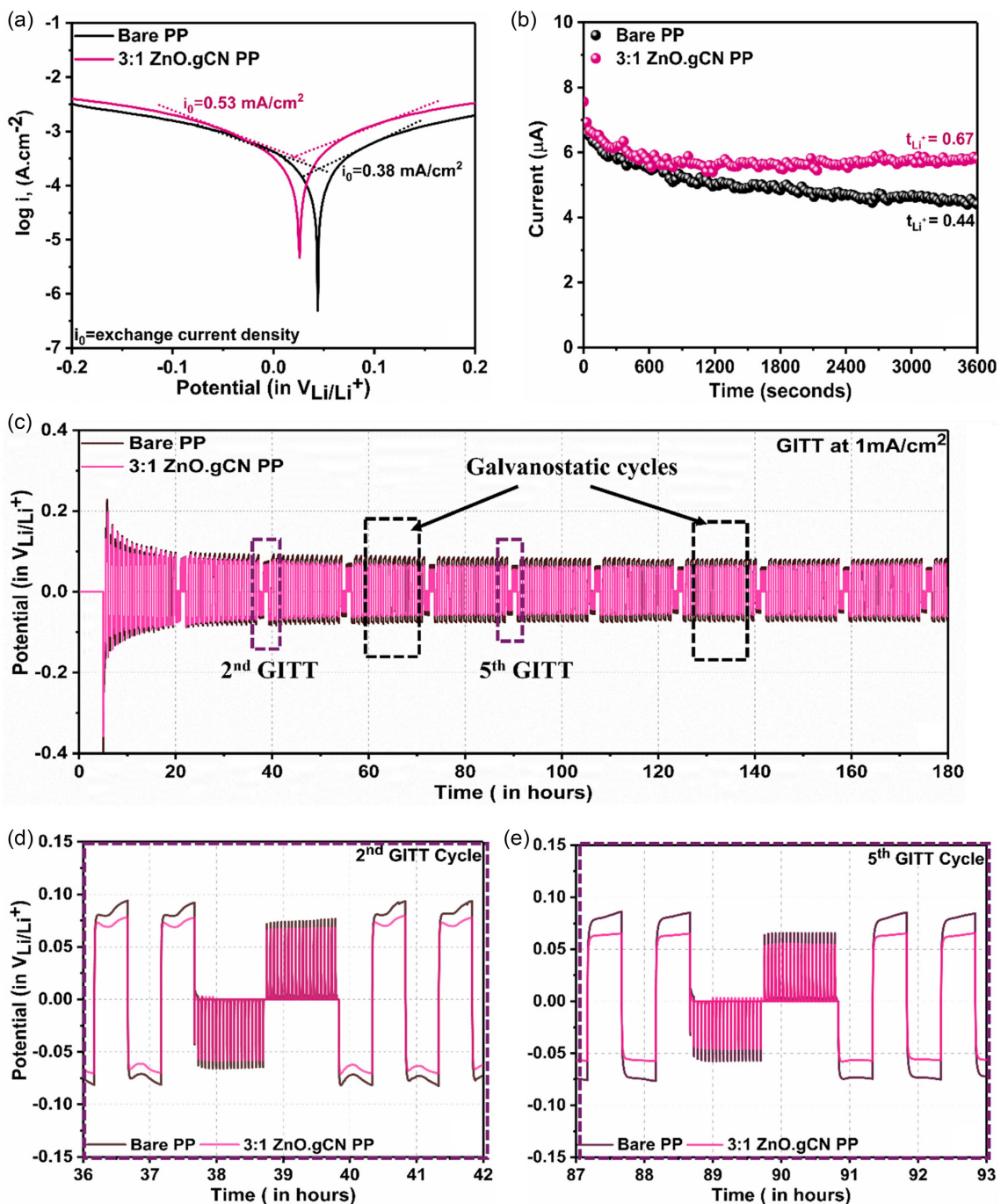


Figure 3. Comparative a) Tafel plots, b) Li ion transference number for bare and 3:1 ZnO.gCN PP, c) GITT voltage-time profiles of Bare PP and 3:1 ZnO.gCN PP, d) GITT 2nd cycle, and e) GITT 5th cycle.

and π -excitations in the gCN heterocycles, while the peak at 398.4 eV is ascribed to the Li-N bond.^[41,42,50] The Li 1s spectra of both cells were deconvoluted into four peaks at 53.9, 54.7, 55.9, and 56.7 eV ascribed to Li_2O , LiOH , Li_2CO_3 , and LiF , respectively. An additional peak in the Li 1s of ZnO.gCN|Li around 55.3 eV was attributed to the inorganic Li-N (Figure 4c,d).^[51] The O 1s spectra of bare Li showed three peaks around 531.4, 532.3, and 533.4 eV corresponding to LiOH , Li_2CO_3 , and $\text{Li}_x\text{PO}_y\text{F}_z$, which are the decomposition products of LiPF_6 and carbonate solvents. The ZnO.gCN|Li exhibits an additional peak

at 530.6 eV, which is related to the Zn-O bond, confirming the presence of ZnO on the Li interphase (Figure S9e, Supporting Information). The deconvoluted F 1s spectra of ZnO.gCN|Li shown in Figure 4e manifested a peak at 686.5 eV, indicating a prominent contribution of ZnF_2 in the SEI compared to what was observed for bare PP.^[52,53] The other three peaks in both cells centered around 685.1, 687.09 and 687.9 eV are attributed to LiF , $\text{Li}_x\text{PO}_y\text{F}_z$, and Li_xPF_y . Also, the P 2p spectra (Figure S9c,d, Supporting Information) deconvolution showed two peaks at 136.6 and 137.56, corresponding to $\text{Li}_x\text{PO}_y\text{F}_z$ and Li_xPF_y . Both

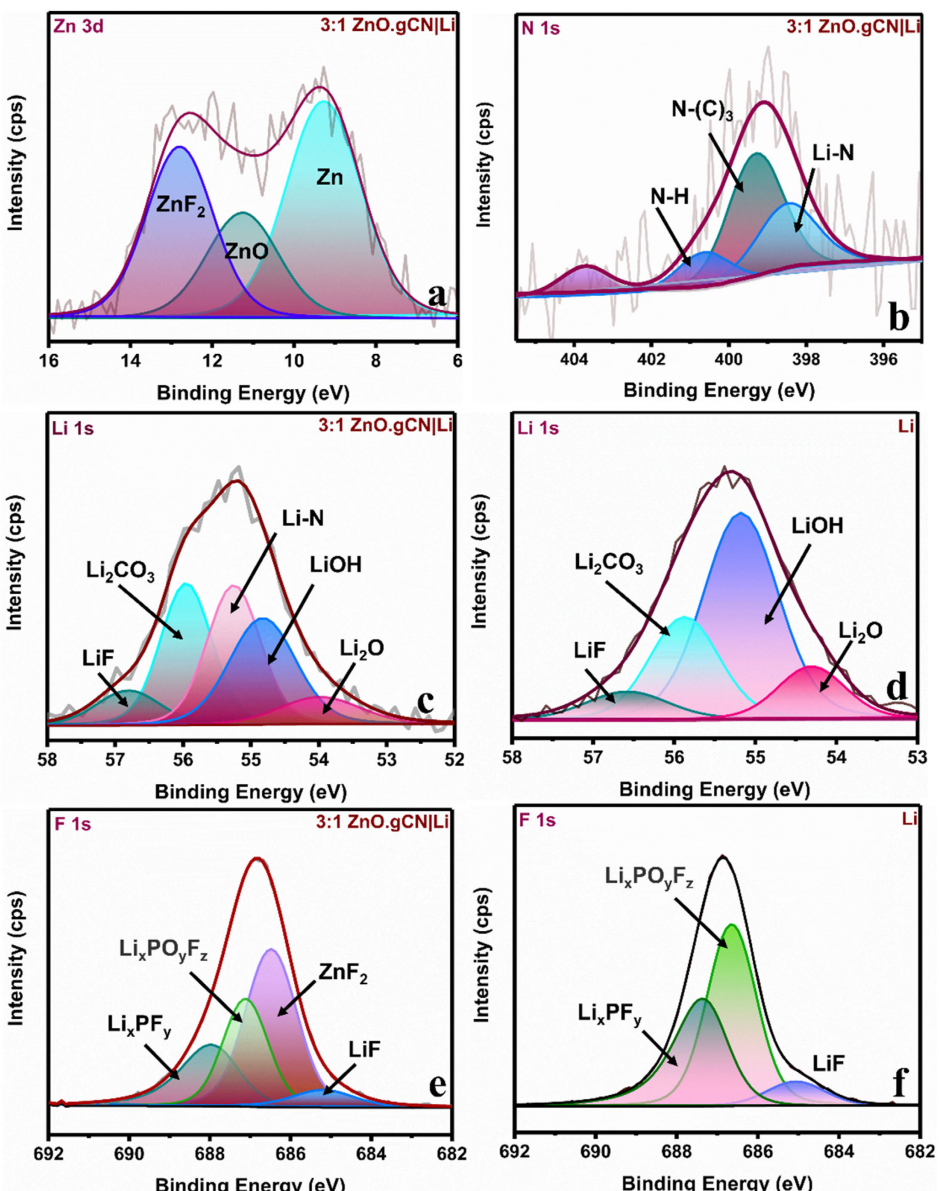


Figure 4. Postcycling a) Zn 3d, b) N 1s, c,d) Li 1s, e,f) F 1s XPS spectra measured on lithium metal anode cycled in the presence of 3:1 ZnO.gCN (a,b,c,e) and Bare PP (d,f).

the F1s and P 2p spectra showed a lower $\text{Li}_x\text{PO}_y\text{F}_z$ to Li_xPF_y ratio in the case of ZnO.gCN|Li compared to bare Li, manifesting suppressed LiPF₆ degradation (Figure S10, Supporting Information). The deconvoluted XPS spectra for C 1s, P 2p, and O 1s are presented in Figure S9, Supporting Information.^[52,53]

From the XPS analysis of the postcycled lithium, it was confirmed that the ZnO.gCN coated separator partially reacted with the lithium metal anode and resulted in ASEI composed of rigid inorganic materials like ZnF₂, gCN, and Li₃N having high shear modulus, thereby contributing toward the mechanical strength and stability of the SEI. The resulting inorganic-rich SEI helped resist dendritic growth during continuous plating striping and suppressed the irreversible electrolyte consumption in SEI repair. Table S1, Supporting Information shows the content of different species that contribute to the formation of inorganic-rich stable SEI.

Next, the HR-SEM images of the cycled lithium were subsequently examined to visually assess the morphology of the lithium anode after 50 plating-stripping cycles. As visible in Figure 5, Bare lithium exhibited highly porous, nonuniform lithium plating. The 3D evolution of the surface depicts the formation of dead lithium. In contrast, the lithium cycled in the presence of 3:1 ZnO.gCN PP (3:1 ZnO.gCN PP) exhibited flat and smooth morphology. The connected smooth surface of plated lithium implied non-preferential lithium plating ascribed to the uniform ion flux and modulated SEI in the presence of a ZnO.gCN coated separator.

The EDX analysis and elemental mapping further confirmed the presence of zinc and nitrogen on the lithium surface, indicating the formation of a Zn and N-enriched SEI in agreement with the XPS analysis (Figure S11, Supporting

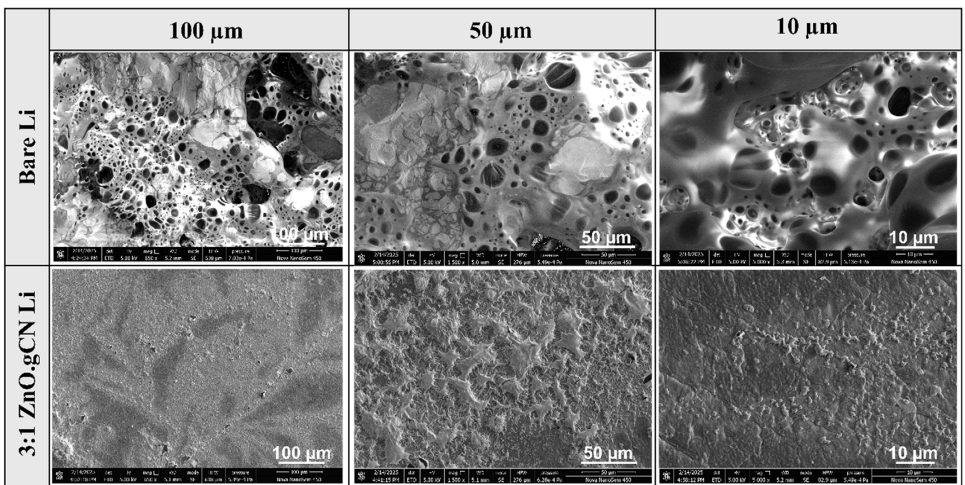


Figure 5. Postcycling HR-SEM image of bare Li and 3:1 ZnO.gCN Li at different resolutions.

Information). This enriched interphase effectively mitigates ongoing electrolyte degradation. It contributes to stabilizing the reactive lithium metal/electrolyte interface, which was also concluded from the lower F and P atomic percentages in 3:1 ZnO.gCN Li. The postcycling HRSEM and XPS

measurements confirmed that the ZnO.gCN-modified separator endows interfacial stability to the metal anode and helps for smooth, uniform lithium metal plating, which explains the superior cycling stability of the ZnO.gCN PP-based Li|Li symmetrical cell.

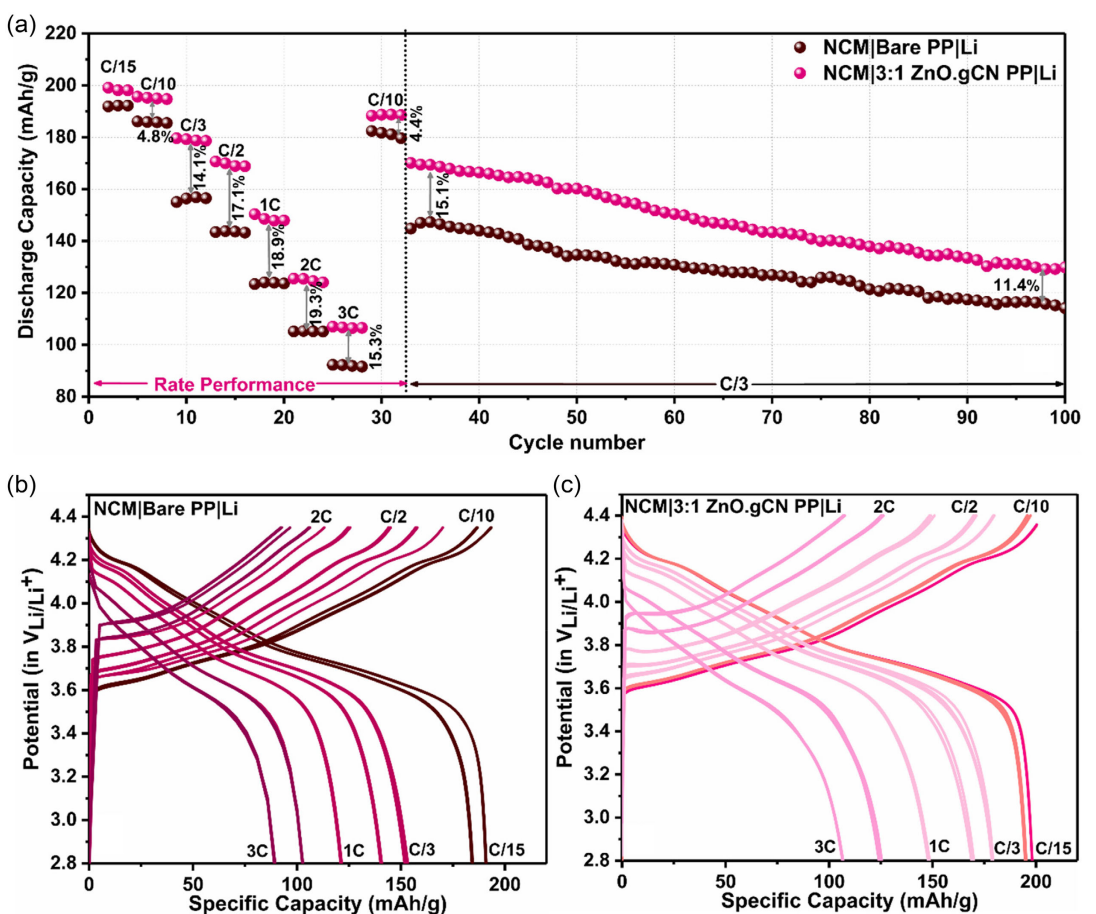


Figure 6. a) Comparative rate performance of NCM|Bare PP|Li and NCM|3:1 ZnO.gCN PP|Li under various current densities from C/15 to 3C and cycling at C/3. Charge-discharge voltage profile corresponding to b) NCM|Bare PP|Li, and c) NCM|3:1 ZnO.gCN PP|Li.

2.4. Lithium Versus NCM

After conducting detailed electrochemical studies and confirming the positive impact of ZnO.gCN on enhancing the stability and reversibility of lithium metal plating and stripping, the performance of the 3:1 ZnO.gCN PP was further assessed in full lithium metal cells using NCM 811 as the cathode. The voltage profiles of the 2nd cycle at C/15 are shown in Figure S12, Supporting Information. The voltage profiles of both cells demonstrated typical electrochemical profiles, indicating that the ZnO.gCN layer is not interfering in the lithiation/delithiation process. For a thorough comparative evaluation, the cells with bare PP (NCM|Bare PP|Li) and 3:1 ZnO.gCN PP (NCM|ZnO.gCN PP|Li) were cycled at increasing C-Rates to examine the influence of superior ionic conductivity and transference number of ZnO.gCN PP on the rate performance of NCM 811. After rate performance, the capacity retention was investigated by cycling the cells at C/10 followed by prolonged cycling at C/3, as depicted in Figure 6a. The figure clearly illustrates that NCM|ZnO.gCN PP|Li exerted enhanced specific capacity across all the C-rates ranging from C/15 to 3C compared to the specific capacity delivered by NCM|Bare PP|Li. Interestingly, the enhancement was more pronounced at faster C-rates owing to the improved Li⁺ transfer and stabilized lithium anode. The NCM|ZnO.gCN PP|Li cells exhibited slightly improved capacity retention at C/10 and C/3 after spanning all the C-rates, delivering nearly 15% higher specific capacity than NCM|Bare-PP|Li. Furthermore, after 100 cycles at a rate of C/3, the NCM|ZnO.gCN PP|Li cells had roughly 11% higher specific capacity (131 mAh g⁻¹) than the NCM|Bare PP|Li cells (112 mAh g⁻¹). Figure 6b,c represents charge-discharge curves of NCM|Bare PP|Li and NCM|ZnO.gCN PP|Li at different rates from C/15 to 3C. The notably enhanced rate performance and increased specific capacity further underscore the effectiveness of the 3:1 ZnO.gCN PP separator in facilitating Li⁺ mass transfer, improving charge transfer kinetics, and stabilizing the electrode/electrolyte interphase in lithium metal-based full-cell configuration.

3. Conclusions

In summary, we successfully fabricated a ZnO.gCN-coated PP separator using a simple and facile binder-free approach. The 3:1 ZnO.gCN coated PP showed greater electrolyte uptake, higher ionic conductivity, and transference number, resulting in improved electrochemical performance. The Li|Li symmetrical cell with 3:1 ZnO.gCN PP exhibited ~2 times lower nucleation overpotential of 113 mV compared to bare PP. Also, 3:1 ZnO.gCN PP enabled stable lithium plating/stripping behavior for more than 500 cycles at a constant current density of 1 mA cm⁻². The Tafel plot and chronoamperometry/EIS analysis demonstrated enhanced exchange current density, lower charge-transfer resistance, and higher Li⁺ transference number in the presence of 3:1 ZnO.gCN PP, indicating facilitated Li⁺ diffusion and modulated Li⁺ flux. GITT experiments conducted to deconvolute the effects of reaction kinetics from mass transport during cycling demonstrated lower voltage peaking behavior, indicating the suppressed dead lithium accumulation in the case of Li|Li symmetrical cell having 3:1

ZnO.gCN PP compared to bare PP cell. The XPS and HR-SEM analysis of post-cycled lithium further revealed that the 3:1 ZnO.gCN PP led to in situ formation of ASEI composed of rigid inorganic materials like ZnF₂, gCN, and Li₃N, having high Young's and shear modulus contributing toward the mechanical strength and stability of the SEI. As a result, the use of ZnO.gCN PP resulted in smooth-uniform deposition and mitigated electrolyte degradation at the interphase, explaining the lower nucleation overpotential, reduced polarization, and remarkable cycling stability. Furthermore, the practicality of 3:1 ZnO.gCN PP was investigated by assembling full cells with NCM 811 as a cathode and lithium metal as the anode. The cells with 3:1 ZnO.gCN PP demonstrated substantially improved rate performance at all rates, showcasing nearly ~15% higher specific capacity at 3C. The simplicity and the economic viability of this study render it advantageous for practical implementations in the stabilization of lithium metal anodes for next-generation high-energy storage systems, such as solid-state and lithium-sulfur batteries.

4. Experimental Section

Materials

All laboratory-grade chemicals, salts, and solvents used in the study were sourced from Sigma Aldrich. The battery-grade lithium foil with a thickness of 0.5 mm, 1 M LiPF₆ in EC: EMC: DMC (1:1:1 volume ratio), and Polypropylene (PP 2500) separators were purchased from MATLABS Technologies, India.

Synthesis of ZnO Nanoplatelets

ZnO nanoplatelets were prepared using the hydrothermal method. A 0.2 M Zn(NO₃)₂·6H₂O solution was mixed with 25 mL of 0.2 M NaOH. The resulting solution was vigorously stirred for 30 min before being transferred to a 100 mL hydrothermal autoclave. The autoclave was subjected to 180 °C for 4 h at a heating rate of 2 °C min⁻¹. After the process, the sample was filtered, rinsed with deionized water, and then dried in a hot-air oven at 100 °C.^[54]

The characterization results of the prepared ZnO nanoplatelets are presented in Figure S1, Supporting Information.

Synthesis of gCN

For the synthesis of gCN, melamine (1.0 g in 40 mL) and cyanuric acid (1.0 g in 20 mL) were dissolved separately in Dimethyl sulfoxide (DMSO). The cyanuric acid solution was then added to the melamine solution, resulting in a white precipitate. The precipitate was left undisturbed for 1 h. Afterward, it was filtered and thoroughly washed with deionized water and ethanol to remove any residual DMSO. The obtained material was dried overnight in a hot-air oven at 80 °C. The dried white precipitate was transferred to an alumina crucible and heated at 500 °C for 5 h with a heating ramp rate of 5 °C min⁻¹. The resulting brown powder was termed as gCN.^[55,56]

The characterization results of the prepared gCN are presented in Figure S1, Supporting Information.

Separator Modification

The synthesized ZnO and gCN were combined in different weight ratios (1:1 ZnO:gCN, 1:3 ZnO:gCN, 3:1 ZnO:gCN) and manually ground

together using a mortar and pestle. Next, a suspension of each composite (1 mg mL^{-1} , i.e., 20 mg in 20 mL of DI water) was prepared. Twenty PP 2500 separators ($\varnothing 18 \text{ mm}$) were immersed in the 20 mL of suspension within a Teflon-lined autoclave maintained at 60°C for 1 h. After this, the separators were removed and vacuum-dried overnight before being used.

Characterization Details: Electrolyte Uptake Studies

For the electrolyte uptake (U) test, the initial weight (W_0) of 18 mm diameter separators, both modified and unmodified, was recorded before and after immersing the separator in a liquid electrolyte (1 M LiPF_6 in EC: EMC: DMC with a 1:1:1 volume ratio) for 1 h. The amount of electrolyte absorbed was then calculated using the following equation:^[57]

$$U (\%) = \left(\frac{W_t - W_0}{W_0} \right) \times 100 \quad (1)$$

where W_t is the weight of a separator after 1 h of immersion in electrolyte; W_0 is the weight of the separator prior to immersion in electrolyte.

Calculation of Ionic conductivity (σ)

The ionic conductivities (σ) of both the unmodified and modified separators were determined using the electrochemical impedance spectroscopy (EIS) method, following the equation:^[58–60]

$$\sigma = \frac{d}{R_b \times A} \quad (2)$$

Here, "A" represents the effective area of the separator, and "d" denotes the distance between the two electrodes, which corresponds to the separator's total thickness. The bulk resistance (R_b) was obtained from the Nyquist plot, recorded within a frequency range of 1 Hz – 100 kHz , using a CHI 660B electrochemical workstation. For the measurement, two electrolyte-soaked separators were placed between two stainless-steel electrodes.

Calculation of Lithium transference number (t_{Li^+})

Lithium transference number (t_{Li^+}) was measured electrochemically following the Vincent–Bruce method.^[61,62]

$$t_{\text{Li}^+} = \frac{I_s(\Delta V - I_0 R_0)}{I_0(\Delta V - I_s R_s)} \quad (3)$$

The initial polarization current (I_0) and steady polarization current (I_s) of the Li|Li symmetrical cells were recorded by the chronoamperometry with a perturbation potential (ΔV) of 10 mV for 3600 s . Meanwhile, the interfacial resistance before and after the polarization (R_0 and R_s) were examined by the EIS.

Instrumentation

The synthesized ZnO, gCN, unmodified and modified separators, along with cycled electrodes, were thoroughly examined using techniques such as X-ray diffraction (XRD), high-resolution scanning electron microscopy (HR-SEM), and X-ray photoelectron spectroscopy (XPS) to assess their structural and morphological characteristics. XRD analysis were conducted using a Rigaku Miniflex 600 X-ray Diffractometer equipped with a Cu-K α radiation source. The scans were performed over the $2\theta = 5$ – 80° range at a scan rate of 2° min^{-1} . HR-SEM pictures and elemental mapping were performed utilizing

the Nova Nano SEM 450 (FEI) equipped with Team Pegasus Integrated EDS-EBSD with Octane Plus and Hikari Pro scanners. The XPS examination used a K-Alpha X-ray photoelectron spectrometer manufactured by Thermo Fisher Scientific. The thermogravimetric analysis (TGA) analysis was performed using the TGA-4000 instrument from PerkinElmer.

Electrochemical Testing

Li|Li symmetrical cells were fabricated in an argon-filled glove box using CR 2032-type coin cells. The assembly included a lithium disc (8 mm diameter) as the cathode and anode with two unmodified and modified Celgard PP 2500 separators (18 mm diameter) and $20 \mu\text{L}$ of electrolyte solution (1 M LiPF_6 in a 1:1:1 vol% mixture of EC, EMC, and DMC). The cells underwent repeated cycling at a constant current, with voltage limits set at $+1.0$ and -1.0 V , across areal current densities ranging from 0.2 to 5 mA cm^{-2} . The charge and discharge duration were kept constant at 30 min for all current densities.

The NCM|Li cells were fabricated by preparing NCM-811 electrodes, which involved mixing NCM-811, carbon black, and PVDF binder (10 wt% in NMP) in a ratio of 80:10:10 using Thinky ARE-310 planetary mixture. The resulting slurry was applied onto battery-grade aluminum foil using a doctor's blade coater set for a wet thickness of $100 \mu\text{m}$, followed by drying at 80°C for 12 h. Afterward, electrodes with a diameter of 12 mm were punched, weighed, and vacuum-dried before assembling into 2032-type coin cells. An average loading of 4 mg cm^{-2} was obtained. The NCM 811 was used as the cathode, Li as the anode, and two Bare PP/3:1 ZnO.gCN PP separators. $20 \mu\text{L}$ of 1 M LiPF_6 EC: EMC: DMC (1:1:1 volume ratio) was used in each cell. The C-rate current requirements were calculated based on a specific capacity of 200 mAh g^{-1} . For all electrochemical tests, the cells were maintained at open-circuit voltage for 5 h. The initial activation cycle was performed at C/15 rate, with the voltage range of 2.8 – 4.4 V .

Postmortem Analysis

After cycling, the cells were decrimped inside the argon-filled glovebox to extract the electrodes and separators for postcycling analysis. The electrodes and separators were washed with dimethyl carbonate and left to dry overnight in the antechamber. HR-SEM and XPS analysis were performed on metal electrodes, minimizing their environmental exposure.

Acknowledgements

R. Y. and A.K.S. contributed equally to this work. R. Y. is grateful to MHRD and IIT (BHU) Varanasi for providing teaching assistantship. A. K. S. is thankful to the University Grant Commission, India, for the Senior Research Fellowship. Rosy acknowledge Science and Engineering Research Board (SERB), India, for the start-up research grant (SRG/2021/000566) and MoE-STARS (2023-0213) for providing the financial support to carry out this project. We acknowledge the CIF at IIT (BHU) Varanasi for providing the advanced instrumentation facilities.

Conflict of Interest

The authors declare no conflict of interest.

Data Availability Statement

The data that support the findings of this study are available on request from the corresponding author. The data are not publicly available due to privacy or ethical restrictions.

Keywords: dendrites · lithium metal anode · modified separators · NCM811 · solid-electrolyte interphase

- [1] S. Kim, G. Park, S. J. Lee, S. Seo, K. Ryu, C. H. Kim, J. W. Choi, *Adv. Mater.* **2023**, *35*, 2206625.
- [2] Z. A. Ghazi, Z. Sun, C. Sun, F. Qi, B. An, F. Li, H.-M. Cheng, *Small* **2019**, *15*, 1900687.
- [3] Q. Wang, B. Liu, Y. Shen, J. Wu, Z. Zhao, C. Zhong, W. Hu, *Adv. Sci.* **2021**, *8*, 2101111.
- [4] J. Wang, B. Ge, H. Li, M. Yang, J. Wang, D. Liu, C. Fernandez, X. Chen, Q. Peng, *Chem. Eng. J.* **2021**, *420*, 129739.
- [5] K. N. Wood, M. Noked, N. P. Dasgupta, *ACS Energy Lett.* **2017**, *2*, 664.
- [6] W. Ren, Y. Zheng, Z. Cui, Y. Tao, B. Li, W. Wang, *Energy Storage Mater.* **2021**, *35*, 157.
- [7] S. T. Oyakhire, H. Gong, Y. Cui, Z. Bao, S. F. Bent, *ACS Energy Lett.* **2022**, *7*, 2540.
- [8] X. Zhang, Y. Yang, Z. Zhou, *Chem. Soc. Rev.* **2020**, *49*, 3040.
- [9] D. Lin, Y. Liu, Y. Cui, *Nat. Nanotechnol.* **2017**, *12*, 194.
- [10] M. S. Whittingham, *Science* **1976**, *192*, 1126.
- [11] S. Xia, C. Yang, Z. Jiang, W. Fan, T. Yuan, Y. Pang, H. Sun, T. Chen, X. Li, S. Zheng, *Adv. Compos. Hybrid Mater.* **2023**, *6*, 198.
- [12] A. Varzi, K. Thanner, R. Scipioni, D. Di Lecce, J. Hassoun, S. Dörfler, H. Altheus, S. Kaskel, C. Prehal, S. A. Freunberger, *J. Power Sources* **2020**, *480*, 228803.
- [13] J. Li, Z. Kong, X. Liu, B. Zheng, Q. H. Fan, E. Garratt, T. Schuelke, K. Wang, H. Xu, H. Jin, *InfoMat* **2021**, *3*, 1333.
- [14] Y. Wu, C. Wang, C. Wang, Y. Zhang, J. Liu, Y. Jin, H. Wang, Q. Zhang, *Mater. Horizons* **2024**, *11*, 388.
- [15] S. Li, M. Jiang, Y. Xie, H. Xu, J. Jia, J. Li, *Adv. Mater.* **2018**, *30*, 1.
- [16] Y. Liu, S. Xiong, J. Wang, X. Jiao, S. Li, C. Zhang, Z. Song, J. Song, *Energy Storage Mater.* **2019**, *19*, 24.
- [17] H. An, Y. Roh, Y. Jo, H. Lee, M. Lim, M. Lee, Y. M. Lee, H. Lee, *Energy Environ. Mater.* **2023**, *6*, e12397.
- [18] Y. Li, Y. Li, L. Zhang, H. Tao, Q. Li, J. Zhang, X. Yang, *J. Energy Chem.* **2023**, *77*, 123.
- [19] S. M. George, *Chem. Rev.* **2010**, *110*, 111.
- [20] C. Ban, S. M. George, *Adv. Mater. Interfaces* **2016**, *3*, 1600762.
- [21] L. Wang, Q. Wang, W. Jia, S. Chen, P. Gao, J. Li, *J. Power Sources* **2017**, *342*, 175.
- [22] N. F. Himma, W. Anita Kusuma, *Polym. Plast. Technol. Eng.* **2017**, *56*, 184.
- [23] U. Siemann, in (Eds: N. Stribeck, B. Smarsly), Solvent cast technology – a versatile tool for thin film production, *Scattering Methods and the Properties of Polymer Materials*. Springer Berlin Heidelberg, Berlin, Heidelberg **2005**, pp. 1–14.
- [24] H. Zhou, S. Yu, H. Liu, P. Liu, *J. Power Sources* **2020**, *450*, 227632.
- [25] R. Xu, X. B. Cheng, C. Yan, X. Q. Zhang, Y. Xiao, C. Z. Zhao, J. Q. Huang, Q. Zhang, *Matter* **2019**, *1*, 317.
- [26] L. Chen, K.-S. Chen, X. Chen, G. Ramirez, Z. Huang, N. R. Geise, H.-G. Steinrück, B. L. Fisher, R. Shahbazian-Yassar, M. F. Toney, M. C. Hersam, J. W. Elam, *ACS Appl. Mater. Interfaces* **2018**, *10*, 26972.
- [27] Y. Sun, Y. Zhao, J. Wang, J. Liang, C. Wang, Q. Sun, X. Lin, K. R. Adair, J. Luo, D. Wang, R. Li, M. Cai, T.-K. Sham, X. Sun, *Adv. Mater.* **2019**, *31*, 1806541.
- [28] E. Cha, M. D. Patel, J. Park, J. Hwang, V. Prasad, K. Cho, W. Choi, *Nat. Nanotechnol.* **2018**, *13*, 337.
- [29] L. Wang, L. Zhang, Q. Wang, W. Li, B. Wu, W. Jia, Y. Wang, J. Li, H. Li, *Energy Storage Mater.* **2018**, *10*, 16.
- [30] X. Wang, M. Zhang, J. Alvarado, S. Wang, M. Sina, B. Lu, J. Bouwer, W. Xu, J. Xiao, J.-G. Zhang, J. Liu, Y. S. Meng, *Nano Lett.* **2017**, *17*, 7606.
- [31] H. Chen, A. Pei, D. Lin, J. Xie, A. Yang, J. Xu, K. Lin, J. Wang, H. Wang, F. Shi, D. Boyle, Y. Cui, *Adv. Energy Mater.* **2019**, *9*, 1900858.
- [32] Y. J. Zhang, W. Wang, H. Tang, W. Q. Bai, X. Ge, X. L. Wang, C. D. Gu, J. P. Tu, *J. Power Sources* **2015**, *277*, 304.
- [33] J. Lang, Y. Long, J. Qu, X. Luo, H. Wei, K. Huang, H. Zhang, L. Qi, Q. Zhang, Z. Li, H. Wu, *Energy Storage Mater.* **2019**, *16*, 85.
- [34] X. Liang, Q. Pang, I. R. Kochetkov, M. S. Sempere, H. Huang, X. Sun, L. F. Nazar, *Nat. Energy* **2017**, *2*, 17119.
- [35] Z. I. Takehara, *J. Power Sources* **1997**, *68*, 82.
- [36] N. S. Choi, Y. M. Lee, W. Seol, J. A. Lee, J. K. Park, *Solid State Ionics* **2004**, *172*, 19.
- [37] Y. Takei, K. Takeno, H. Morimoto, S. I. Tobishima, *J. Power Sources* **2013**, *228*, 32.
- [38] Y. Xiang, J. Li, J. Lei, D. Liu, Z. Xie, D. Qu, K. Li, T. Deng, H. Tang, *ChemSusChem* **2016**, *9*, 3023.
- [39] Y. Ouyang, C. Cui, Y. Guo, Y. Wei, T. Zhai, H. Li, *ACS Appl. Mater. Interfaces* **2020**, *12*, 25818.
- [40] H. Qian, X. Li, Q. Chen, W. Liu, Z. Zhao, Z. Ma, Y. Cao, J. Wang, W. Li, K. Xu, K. Zhang, W. Yan, J. Zhang, X. Li, *Adv. Funct. Mater.* **2024**, *34*, 2310143.
- [41] Y. Guo, P. Niu, Y. Liu, Y. Ouyang, D. Li, T. Zhai, H. Li, Y. Cui, *Adv. Mater.* **2019**, *31*, 1900342.
- [42] C. Jiao, H.-B. Sun, L. Zhang, S.-Q. Zhao, G.-Y. Pang, C.-R. Zhao, S.-G. Lu, *Rare Met.* **2024**, *43*, 1030.
- [43] X. Wang, Z. Chen, X. Xue, J. Wang, Y. Wang, D. Bresser, X. Liu, M. Chen, S. Passerini, *Nano Energy* **2025**, *133*, 110439.
- [44] S. Han, B. Wu, H. Wang, P. Wen, L. Zhang, X. Lin, M. Chen, *Angew. Chem. Int. Ed.* **2023**, *62*, e202308724.
- [45] T. R. Jow, S. A. Delp, J. L. Allen, J.-P. Jones, M. C. Smart, *J. Electrochem. Soc.* **2018**, *165*, A361.
- [46] W. Cai, Y. Gao, W. Feng, J. Xu, M. Wang, J. Sun, M. Cao, Z. Qu, X. Liu, X. Huang, H. Zhou, Z. Huang, *Small* **2024**, *2403831*, 1.
- [47] X. Wang, S. Wang, H. Wang, W. Tu, Y. Zhao, S. Li, Q. Liu, J. Wu, Y. Fu, C. Han, F. Kang, B. Li, *Adv. Mater.* **2021**, *33*, 1.
- [48] K. H. Chen, K. N. Wood, E. Kazayak, W. S. Lepage, A. L. Davis, A. J. Sanchez, N. P. Dasgupta, *J. Mater. Chem. A* **2017**, *5*, 11671.
- [49] V. Der Laan, *Phys. Rev. B* **1981**, *23*, 4369.
- [50] F. Yu, L. Wang, Q. Xing, D. Wang, X. Jiang, G. Li, A. Zheng, F. Ai, J. P. Zou, *Chinese Chem. Lett.* **2020**, *31*, 1648.
- [51] S. Ishiyama, Y. Baba, R. Fujii, M. Nakamura, Y. Imahori, *Nippon Kinzoku Gakkaishi/Journal Japan Inst. Met.* **2014**, *78*, 137.
- [52] F. Li, J. He, J. Liu, M. Wu, Y. Hou, H. Wang, S. Qi, Q. Liu, J. Hu, J. Ma, *Angew. Chem. Int. Ed.* **2021**, *60*, 6600.
- [53] B. S. Parimalam, A. D. MacIntosh, R. Kadam, B. L. Lucht, *J. Phys. Chem. C* **2017**, *121*, 22733.
- [54] K. Sahu, A. K. Kar, *Mater. Sci. Semicond. Process.* **2019**, *104*, 104648.
- [55] Y.-S. Jun, E. Z. Lee, X. Wang, W. H. Hong, G. D. Stucky, A. Thomas, *Adv. Funct. Mater.* **2013**, *23*, 3661.
- [56] Y. Duan, X. Li, K. Lv, L. Zhao, Y. Liu, *Appl. Surf. Sci.* **2019**, *492*, 166.
- [57] J. Cao, D. Zhang, X. Zhang, M. Sawangphruk, J. Qin, R. Liu, *J. Mater. Chem. A* **2020**, *8*, 9331.
- [58] C. Sun, Y. Li, J. Jin, J. Yang, Z. Wen, *J. Mater. Chem. A* **2019**, *7*, 7752.
- [59] D. Lee, I. Hwang, Y. Jung, S. Sun, T. Song, U. Paik, *J. Alloys Compd.* **2021**, *885*, 161157.
- [60] S. Choi, S. Mugobera, J. M. Ko, K. S. Lee, *Colloids Surf. A* **2021**, *631*, 127722.
- [61] J. Evans, C. A. Vincent, P. G. Bruce, *Polymer* **1987**, *28*, 2324.
- [62] S. Zugmann, M. Fleischmann, M. Amereller, R. M. Gschwind, H. D. Wiemhöfer, H. J. Gores, *Electrochim. Acta* **2011**, *56*, 3926.

Manuscript received: February 23, 2025

Revised manuscript received: April 24, 2025

Version of record online: May 6, 2025